ACS APPLIED MATERIALS & INTERFACES

Research Article

www.acsami.org

Extraordinary Improvement of Gas-Sensing Performances in SnO_2 Nanofibers Due to Creation of Local *p*−*n* Heterojunctions by Loading Reduced Graphene Oxide Nanosheets

Jae-Hyoung Lee,[†] Akash Katoch,[†] Sun-Woo Choi,[†] Jae-Hun Kim,[†] Hyoun Woo Kim,*[,‡] and Sang Sub Kim*[,†]

[†]Department of Materials Science and Engineering, Inha University, Incheon 402-751, Republic of Korea

[‡]Division of Materials Science and Engineering, Hanyang University, Seoul 133-791, Republic of Korea

Supporting Information

ABSTRACT: We propose a novel approach to improve the gas-sensing properties of *n*-type nanofibers (NFs) that involves creation of local *p*−*n* heterojunctions with *p*-type reduced graphene oxide (RGO) nanosheets (NSs). This work investigates the sensing behaviors of *n*-SnO_2 NFs loaded with *p*-RGO NSs as a model system. *n*-SnO_2 NFs demonstrated greatly improved gas-sensing performances when loaded with an optimized amount of *p*-RGO NSs. Loading an optimized amount of RGOs resulted in a 20-fold higher sensor response than that of pristine SnO_2 NFs. The sensing mechanism of monolithic SnO_2 NFs is based on the joint effects of modulation of the potential barrier at nanograin boundaries and radial modulation of the electron-depletion layer. In addition to the sensing mechanisms described above, enhanced sensing was obtained for *p*-RGO NS-loaded SnO_2 NFs due to creation of local *p*−*n* heterojunctions, which not only provided a potential barrier, but also functioned as a local electron absorption reservoir. These mechanisms markedly increased the resistance of SnO_2 NFs, and were the origin of intensified resistance modulation during interaction of analyte gases with preadsorbed oxygen species or with the surfaces and grain boundaries of NFs. The approach used in this work can be used to fabricate sensitive gas sensors based on *n*-type NFs.

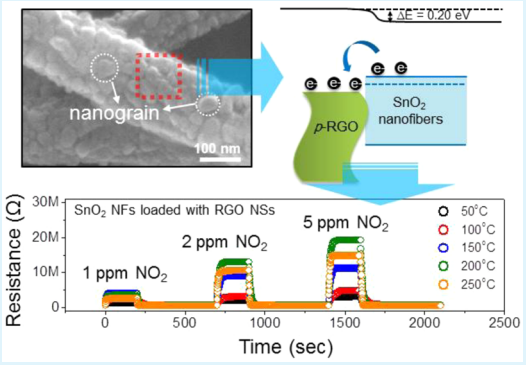

KEYWORDS: *sensing mechanism, SnO_2 nanofibers, reduced graphene oxide, electronic sensitization*

1. INTRODUCTION

One-dimensional (1D) semiconductor oxide structures have been intensively studied for gas sensing applications for several reasons. The 1D morphology of these structures is suitable for directional carrier transport. Second, the structures have size confinement along two coordinates and hence the smallest dimension, which is most efficient for translating gas recognition into an electrical signal.[1,2] Third, because of their high surface-to-volume ratio, nearly the entire bulk of these materials is readily affected by gas molecules. Fourth, these structures are relatively easy to integrate at low cost. Accordingly, tremendous efforts have been dedicated to synthesizing 1D structures and characterizing their gas sensing performances.

Among a variety of 1D nanostructures, electrospun nanofibers (NFs) have extraordinary sensing characteristics, which have been ascribed to efficient diffusion of gas molecules through a web-like structure of NFs.[3] In addition, the polycrystalline nature of electrospun NFs, which consist of many grains, provides potential barriers between grains within NFs in addition to those between individual NFs.[4] In particular, electrospun NFs are easily produced on a large scale due to the facile preparation process.[5]

Tin dioxide (SnO_2) is a well-known *n*-type wide band gap semiconductor (E_g = 3.6 eV, at 300 K). Due to its attractive characteristics such as nontoxicity, low-cost preparation, and simple fabrication, SnO_2 is regarded as one of the most promising sensing materials to detect a wide variety of pollutant gases.[6,7] Accordingly, SnO_2 electrospun NFs are promising candidates for gas sensors. To improve the sensing characteristics of SnO_2 NFs, functionalization techniques such as Al doping,[8] Pt doping,[9] CuO−SnO_2 composites,[10] In_2O_3−SnO_2 composites,[11] and loading of $La_{0.7}Sr_{0.3}FeO_3$ nanoparticles[12] have been investigated.

Heterostructures based on semiconductors have been fabricated for use in advanced gas-sensor applications. Basu et al. reported that a Pd/ZnO interface provided a site for the adsorption of H_2 gas and the subsequent chemical reaction, which increased the current flow and thus the sensitivity of the sensor relative a sensor without a Pd/ZnO interface.[13] In a CuO/ZnO thin-film heterojunction, the generated interface states have been shown to affect current flow.[14] Ling et al.

Received: October 17, 2014
Accepted: January 20, 2015
Published: January 20, 2015

DOI: 10.1021/am5071656
ACS Appl. Mater. Interfaces 2015, 7, 3101−3109

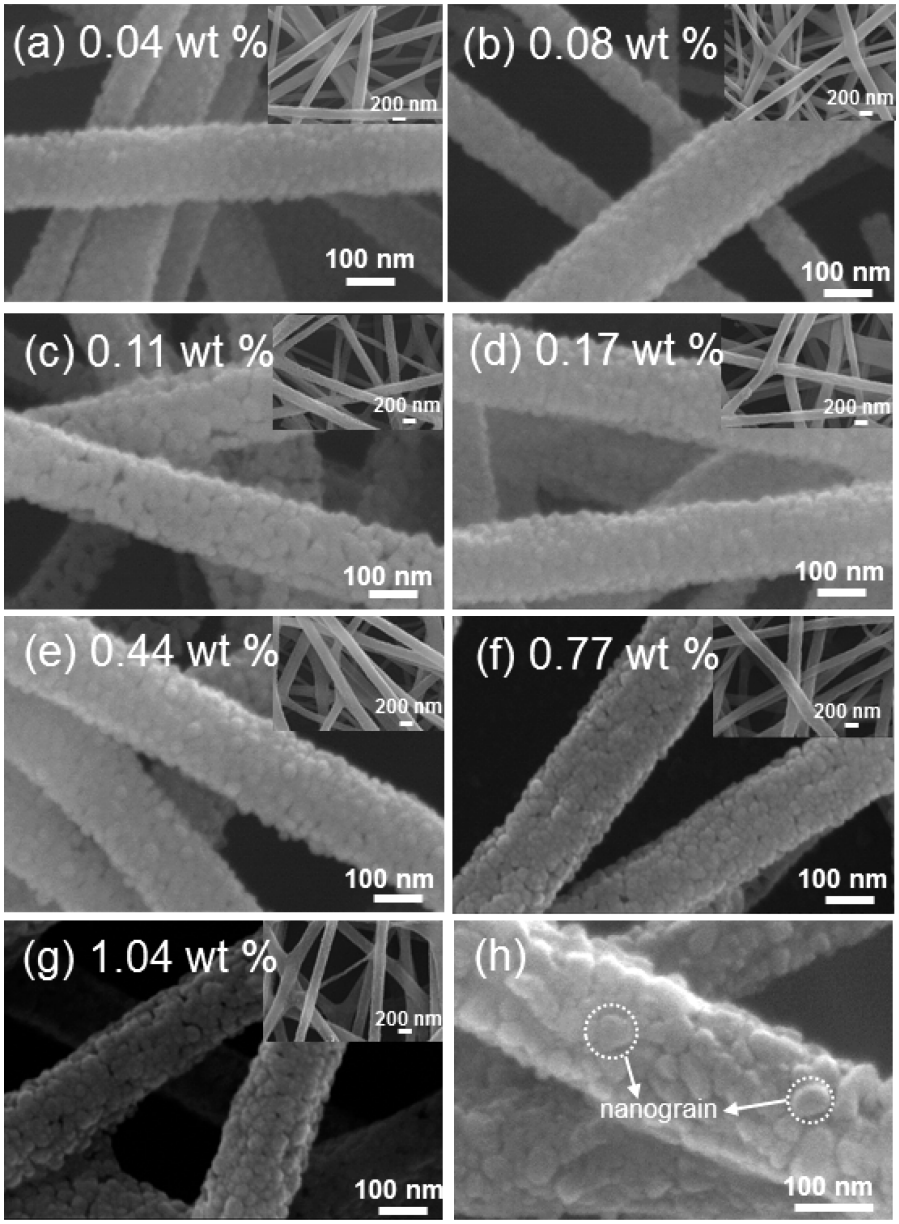

Figure 1. SEM images of RGO NSs-loaded SnO_2 NFs with the *p*-RGO NSs-content of (a) 0.04, (b) 0.08, (c) 0.11, (d) 0.17, (e) 0.44, (f) 0.77, and (g) 1.04 wt % (upper right inset: low-magnification SEM images). (h) Enlarged SEM image exhibiting a typical morphology of nanograins in NFs.

found that *n*-ZnO/*p*-$BaTiO_3$−CuO−La_2O_3 combined the responses of the individual metal oxides (i.e., *n*-type and *p*-type) with that of the heterojunction, improving overall sensing performance.[15] *p*-CuO/*n*-ZnO heterojunctions have also been intensively studied as promising sensors.[16,17] In addition, Huang et al. recently reported *n*-ZnO/*n*-SnO_2 heterojunctions, in which SnO_2 nanorods were modified with ZnO thin films or nanoparticles.[18] In this case, an *n*−*p*−*n* sensing response resulting from the unique morphology and dimensions of the structure was observed. As above-mentioned, the use of *p*−*n* heterostructures is a novel approach to improving the gas-sensing capabilities of monolithic sensor materials. We therefore synthesized SnO_2 electrospun NFs and investigated the application of *p*−*n* heterostructures in these NFs.

In particular, we loaded *p*-reduced graphene oxide nanosheets (RGO NSs) on electrospun SnO_2 NFs. Ding et al. reported unique SnO_2/RGO hybrid structure, showing greatly enhanced lithium storage properties compared to the pure SnO_2 NSs.[19] The possibility of using RGOs as a chemical sensor was examined in a previous study.[20] Several research groups reported that pristine RGO can be used to detect NO_2,[21] NH_3,[21] and organic vapors.[22] Recently, Deng et al. devised RGO-conjugated Cu_2O nanowire mesocrystals with increased surface area and conductivity that had high sensitivity to NO_2 gas, and proposed the concept of RGO-containing composite sensors.[23]

We hypothesized that an *n*-type SnO_2/*p*-type RGO configuration would result in enhanced sensing behavior. There have been numerous papers on the nanocomposites of SnO_2/reduced graphene oxides (RGO). For most previous works, SnO_2 nanoparticles/nanocrystals were anchored on RGO NSs[24−33] or on RGO nanoribbones.[34] They have been used as anodes for lithium ion batteries,[24,25,30,31,34] electrochemical sensors,[26,32] NO_2 gas sensors,[27,29] glucose sensors,[33] and humidity sensors.[28] Choi et al. fabricated the nanocomposites, in which SnO_2 NFs were embedded onto the RGO

DOI: 10.1021/am5071656
ACS Appl. Mater. Interfaces 2015, 7, 3101−3109

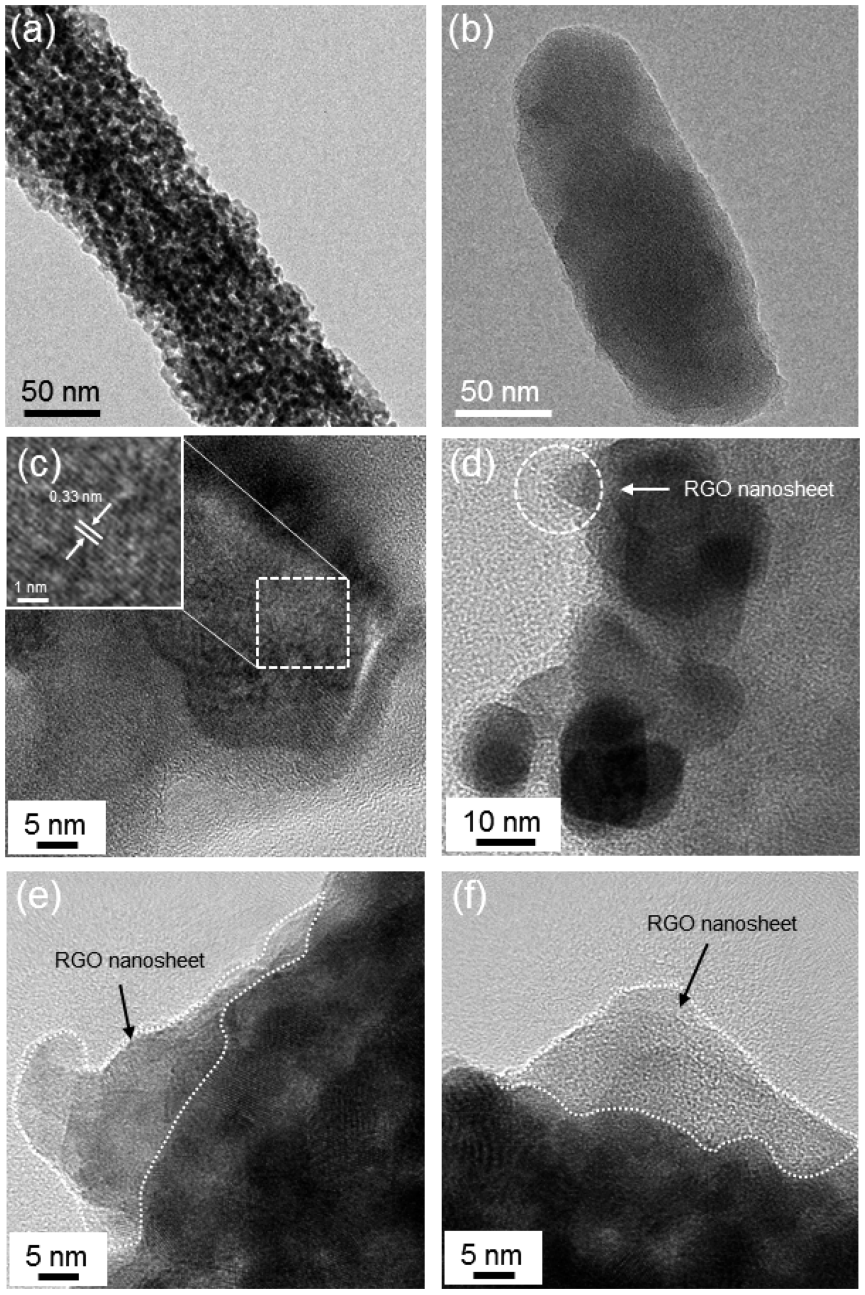

Figure 2. (a) Low-magnification TEM image of a RGO NSs-loaded SnO_2 NF. (b) High-resolution TEM image taken from an RGO NS, prior to loading. (c,d) High-magnification TEM images which enlarge the areas (c) in the SnO_2 nanocrystals and (d) in the RGO NSs in a RGO NSs-loaded SnO_2 NF. (e,f) Lattice-resolved TEM images exhibiting the loaded RGO NSs.

NSs, detecting acetone and H_2S gases.[35] Although the surfaces of RGOs and SnO_2 NFs were directly contacted in Choi et al.'s nanocomposites, the RGO NSs in the present work exist not only on the surface of SnO_2 NFs but also inside the NFs. Furthermore, in the present work, the nanocomposites exhibited the most drastic improvement of sensing behavior, selectively to NO_2 gas.

In this study, we prepared *p*-RGO NS-loaded SnO_2 NFs using a simple electrospinning method. Previous studies of heterostructure sensors took advantage of the various properties of heterojunctions, such as their self-cleaning properties,[13] generation of interfacial states,[14] and change of current flow through heterojunctions.[15−17] In contrast, the sensing mechanism in our synthesized NFs is based on the effects of radial modulation of the electron-depletion layer along the heterojunction, in addition to modulation of potential barriers at nanograin boundaries due to the nature of electrospun NFs. The extraordinary improvement in sensing behavior that we obtained can be applied to other sensor devices, paving the way for further development of high-quality semiconductor sensors.

2. EXPERIMENTAL SECTION

Materials. Tin(II) chloride dihydrate ($SnCl_2{\cdot}2H_2O$, Sigma-Aldrich Corp.), reduced graphene oxide NSs (*p*-RGO NSs), polyvinyl acetate (PVAc, Mw = 850 000, Sigma-Aldrich Corp.), ethanol (anhydrous, 99.5%, Sigma-Aldrich Corp.), and dimethylformamide (DMF, anhydrous, 99.8%, Sigma-Aldrich Corp.) were used as received, without further purification.

DOI: 10.1021/am5071656
ACS Appl. Mater. Interfaces 2015, 7, 3101−3109

Synthesis of *p*-RGO NS-Loaded SnO_2 NFs. The procedure used to synthesize *p*-RGO NS-loaded SnO_2 NFs using electrospinning is as follows. First, PVAc was dissolved in mixed solvent consisting of ethanol (20 g) and DMF (15 g). Subsequently, $SnCl_2{\cdot}2H_2O$ (2.7 g) and *p*-RGO NSs 0.04 wt % (0.0007 g) were added to the PVAc solution, and the solution stirred for 10 h. The average size of the as-prepared *p*-RGO NS was estimated to be about 75 nm (Figure S1, Supporting Information). The prepared viscous solution was loaded into a syringe equipped with a 21-gauge stainless steel needle with an inner diameter of 0.51 mm. Feed rate, applied voltage, and distance between the tip of the needle and the collector were fixed at 0.03 mL/h, 15 kV, and 20 cm, respectively. All experiments were performed at room temperature in air. As-spun NFs were collected over SiO_2-grown (thickness ~250 nm) Si wafers that were placed on the collector. The prepared as-spun NFs were calcined at 650 °C in air for 2 h at a heating rate of 2 °C/min. Previous literature reveals that the RGO will be stable at temperatures in the range of −10 to +800 °C.[36,37] Accordingly, the *p*-RGO NS will be stable during the sintering process at 650 °C. *p*-RGO NSs-loaded SnO_2 NFs with different contents (*p*-RGO NSs; 0.04−1.04 wt %) were also synthesized using the above-mentioned procedure. Details of the procedure adopted for the synthesis of SnO_2 NFs are provided in our earlier report.[38] We estimated the surface area of the NFs by means of using the Brunauer−Emmett−Teller (BET) equation.

Microstructural Analysis and Sensing Measurements. Microstructure and phase composition of the synthesized *p*-RGO NS-loaded SnO_2 NFs were investigated by scanning electron microscopy (SEM, Hitachi S-4200) and transmission electron microscopy (TEM, Philips CM-200). To investigate the sensing behavior of *p*-RGO NS-loaded SnO_2 NFs, double layer electrodes of Au (thickness ~200 nm) and Ti (thickness ~50 nm) were sequentially sputter-deposited on specimens using an interdigitated electrode mask. The response of the *p*-RGO NS-loaded SnO_2 NF sensors to oxidizing gases (NO_2, SO_2, O_2) and reducing gases (H_2, CO, C_7H_8, C_6H_6) was measured using a homemade gas dilution and sensing system. In Figure S2 of the Supporting Information, we showed a top-view SEM image taken from a RGO NS-loaded SnO_2 NFs sample, on which the electrode layer was deposited. It clearly exhibits the boundary between the electrode layer (the light gray area in the figure) and RGO NS-loaded SnO_2 NFs (the dark gray area). Thermogravimetric analysis (TGA) was tested on STA 409 PC (NETZSCH).

The rates of weight loss of pure RGO and RGO NS-loaded SnO_2 NFs, as measured by the TGA, are shown in Supporting Information (Figure S3). In the case of RGO NS-loaded SnO_2 NFs, the higher rates of weight loss were observed between 150 and 200 °C, 320−400 °C, and 550−600 °C, respectively. The weight loss between 150 and 200 °C will come from the evaporation of physically adsorbed water and NH_3 gas.[39] On the other hand, no significant weight loss was observed up to 900 °C, in the case of pure RGO NSs.

Details of sensor design, gas dilution, and the sensing system are provided in our earlier reports.[40−43] Gas concentration was controlled by changing the mixing ratio of the dry air-balanced target gas and dry air through accurate mass flow controllers. Total flow rate was set to 500 sccm to avoid any possible variation in sensing properties. Sensing characteristics at various different gas concentrations were evaluated at 1, 2, and 5 ppm at various operating temperatures. Gas response for oxidizing gases (reducing gases) was evaluated as R_g/R_a (R_a/R_g), where R_a is the resistance of the sensor in air and R_g is the resistance of the sensor in the presence of the applied gas.

3. RESULTS

Representative FE-SEM images of RGO NS-loaded SnO_2 NFs are shown in Figure 1. The corresponding low-magnification images of the NFs, shown as insets in each figure, show the random and uniform distribution of NFs on the substrates, indicating that there was no difference in connectivity and overall distribution of NFs with regard to the amount of loaded RGO NSs. The average diameter of NFs was ~180 nm for all NFs, regardless of the amount of RGO NSs present. It is noteworthy that individual NFs consisted of nanosized grains, namely nanograins. The typical morphology of a nanograin is shown in Figure 1h. In Figure S4 (Supporting Information), we present more clear SEM images, showing the nanograins and the RGO NSs-comprising regions.

Evolution of nanograins in oxide NFs has been thoroughly investigated.[44−46] The activation energies of nanograins are 1 order of magnitude smaller than their bulk counterparts.[44,46] Investigation of their isothermal growth behaviors revealed that their predominant growth mechanisms are lattice and/or surface diffusion.[44−47] The size of nanograins has been found to greatly influence the properties of NFs, such as their gas sensing ability,[44,45,48,49] optical bandgap,[50−53] and magnetism.[54−56] The nanograin size of RGO NS-loaded SnO_2 NFs was ~30 nm irrespective of the amount of RGO NSs present, suggesting that loading of RGO NSs does not noticeably affect the growth of nanograins.

The microstructure of RGO NSs-loaded SnO_2 NFs with 0.44 wt % RGO NSs was further investigated by TEM. The low-magnification TEM image shown in Figure 2a clearly shows the presence of nanograins in the single NF, highlighting the polycrystalline nature of nanograins. This is in good agreement with the FE-SEM image shown in Figure 1. The high-resolution image taken from a RGO NS prior to loading is shown in Figure 2b. Several overlapping RGO sheets were observed. The high-magnification TEM image shown in Figure 2c reveals clearly SnO_2 nanocrystals. The interplanar distance of 0.33 nm noted in the figure corresponds to the (110) plane of tetragonal SnO_2. Figure 2d shows agglomeration of SnO_2 nanograins on part of the NFs, and a RGO NS, which is noted in the figure. Figure 2e,f shows that some RGO NSs were exposed on the surfaces of NFs.

We first investigated the NO_2-sensing performances of the prepared RGO NS-loaded SnO_2 NFs according to RGO NS content. Typical resistance curves measured at 50−250 °C for 1, 5, and 10 ppm of NO_2 are shown in Figure 3. All sensors clearly tracked the change in NO_2 gas concentration. The resistance increased/decreased during the supply/stoppage of NO_2, respectively. This overall sensing behavior can be explained from the perspective of *n*-type oxide semiconductors. It is noteworthy that RGO NS-loaded SnO_2 NFs showed detectable resistance variation even at the very low operating temperature of 50 °C, suggesting that they have potential for use in low-power, polymer-compatible NO_2 sensors. The corresponding NO_2 responses of the RGO NS-loaded SnO_2 NFs for 5 ppm of NO_2 are summarized in Figure 4. Sensor responses increased with increasing operating temperature, and reached maximum values at 200 °C. However, a further increase in the operating temperature tended to decrease the responses. This bell-shape behavior of gas responses is very common in oxide semiconducting-type chemiresistor sensors.[57] Figure 4b shows the change in sensor response as a function of the amount of RGO NSs loaded at the operating temperature of 200 °C. The NO_2 concentration was set to 5 ppm. The best NO_2-sensing performance was obtained at the optimal RGO NS amount of 0.44 wt %. The same behavior was observed at the other operating temperatures examined. To avoid repetition, these data are not included. For the sake of comparison, the NO_2-sensing response of pure SnO_2 NF at 5 ppm is included.[38] In addition, we presented the results, testing the sensor responses of the pristine SnO_2 NFs to NO_2 in the range of 1−5 ppm at 200 °C (Figure S5, Supporting

DOI: 10.1021/am5071656
ACS Appl. Mater. Interfaces 2015, 7, 3101−3109

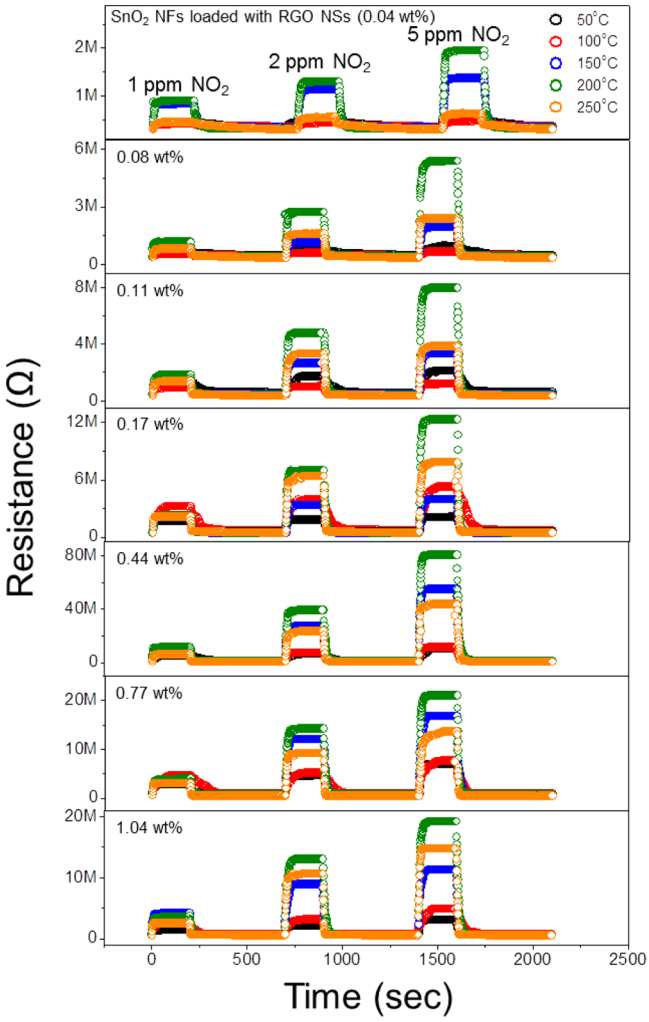

Figure 3. Dynamic response curves measured from RGO NSs-loaded SnO_2 NFs with the *p*-RGO NSs-content of 0.04, 0.08, 0.11, 0.17, 0.44, 0.77, and 1.04 wt %, respectively. Each curve was plotted for NO_2 concentration of 1, 2, and 5 ppm, respectively, at temperatures in the range of 50−250 °C.

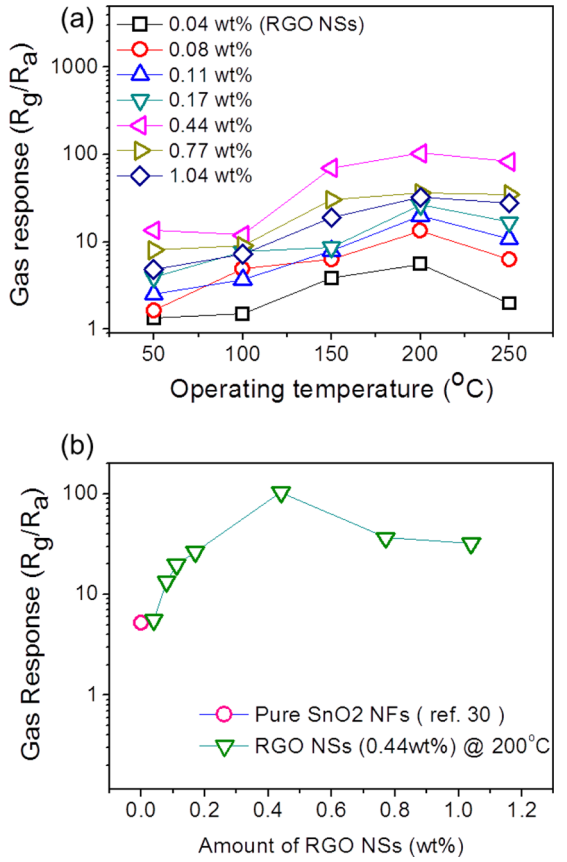

Figure 4. Changes of sensor responses by varying (a) operating temperature and (b) amount of RGO NSs. The NO_2 concentration was set to 5 ppm.

Information). It is clear that loading of RGO NSs greatly improved NO_2 sensor response.

Sensing abilities of the RGO NS-loaded SnO_2 NFs with RGO NS 0.44 wt %, which was the optimized RGO NS content, for other oxidizing gases such as SO_2 and O_2 were investigated, and the results are shown in Figure 5. Dynamic resistance curves in Figure 5a and the summarized gas responses in Figure 5b indicate that the sensor exhibited better sensing behavior toward NO_2 than the other oxidizing gases. The exceptionally high response to NO_2 is likely not related to the selective NO_2-sensing ability of RGO NS-loaded SnO_2 NFs, but rather the high reactivity of NO_2 molecules to general sensor materials. Numerous studies[57−59] have reported high NO_2 sensing by a broad array of sensor materials.

In addition, sensing tests were performed with 0.44 wt %-RGO NS-loaded SnO_2 NFs for various reducing gases such as H_2, CO, C_7H_8, and C_6H_6. Dynamic resistance curves for the tested gases are shown in Figure 6a. The sensor fabricated with RGO NS-loaded SnO_2 NFs with RGO NSs 0.44 wt % demonstrated typical *n*-type semiconducting sensor behavior in response to reducing gases; reaction between reducing gases and preadsorbed oxygen species tends to produce volatile molecules, resulting in the removal of preadsorbed oxygen species on the surface of the sensor materials; this returns captured electrons to the conduction band of *n*-type semiconductors, decreasing resistance. As summarized in Figure 6b, the responses to the tested reducing gases were superior to those of pure SnO_2 NFs.[38]

4. DISCUSSION

Collectively, our results show that loading of RGO NSs into SnO_2 NFs is an effective approach to improve both the oxidizing and reducing gas-sensing performances of pure SnO_2 NFs. The loading amount needs to be optimized to ensure the best sensing properties; loading lower or higher contents of RGO NSs than the critical amount has an adverse effect on the gas-sensing properties of SnO_2 NFs.

To gain a better understanding of the sensing mechanism operating in RGO NS-loaded SnO_2 NFs, we first describe the sensing mechanism of monolithic (i.e., pure SnO_2) NFs. Sensing is based on the joint effects of two resistance modulations. One is resistance modulation due to changes in the potential barrier established at nanograin boundaries. This is the universal sensing mechanism that operates in polycrystalline oxide semiconducting sensor materials. At grain boundaries, oxygen species in air diffuse along the grain boundary in the polycrystalline sensor material, and build up upward band bending in the case of *n*-type semiconductors, functioning as a barrier to electron transport along the applied electric field. The potential barrier increases or decreases due to interdiffusion of oxidizing gas molecules or outdiffusion of

DOI: 10.1021/am5071656
ACS Appl. Mater. Interfaces 2015, 7, 3101−3109

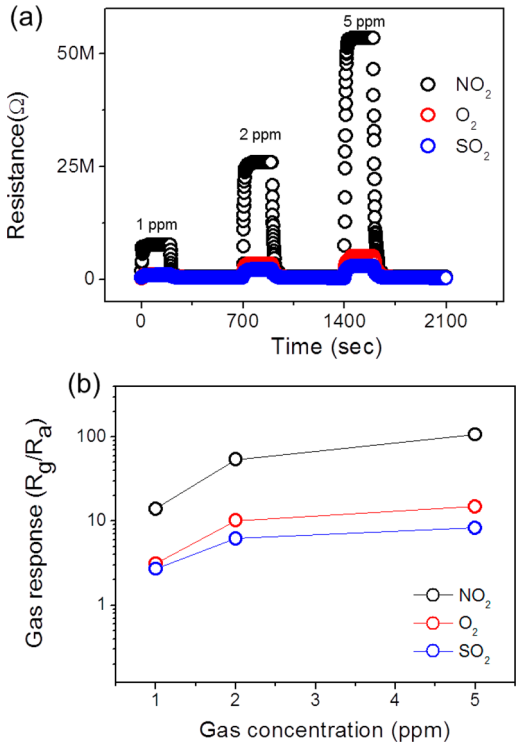

Figure 5. (a) Dynamic response curves for NO_2, O_2, and SO_2 gases. The concentration was set to of 1, 2, and 5 ppm, respectively. (b) Change of sensor responses by varying the gas concentration in the range of 1−5 ppm, for NO_2, O_2, and SO_2 gases.

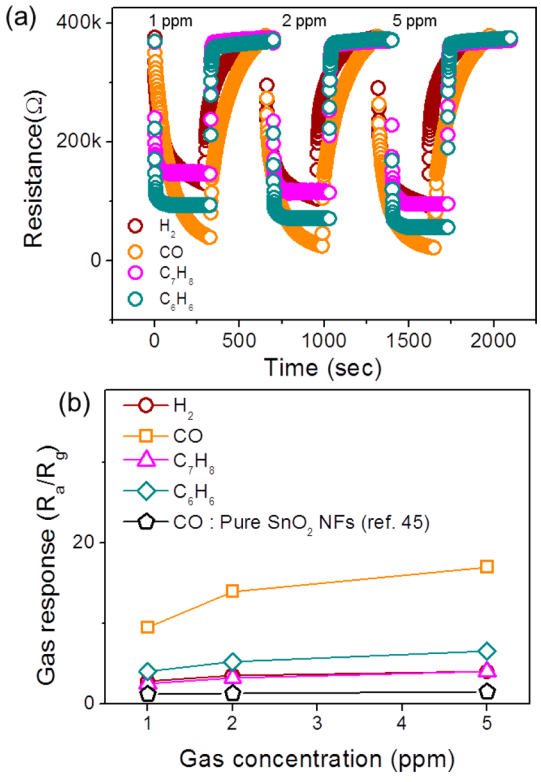

Figure 6. (a) Dynamic response curves for H_2, CO, C_7H_8, and C_6H_6 gases. The concentration was set to of 1, 2, and 5 ppm, respectively. (b) Change of sensor responses by varying the gas concentration in the range of 1−5 ppm, for H_2, CO, C_7H_8, and C_6H_6 gases.

preadsorbed oxygen species under a reducing gas environment, respectively. The other modulation source is radial modulation of the electron-depletion layer in SnO_2 NFs. It is well-known that 1D nanomaterials, including nanowires, have an electron-depletion layer underneath the surface due to capture of electrons in the conduction band of *n*-type semiconductors by adsorbed oxygen species. This electron-depletion layer modulates radially; expansion or suppression of the electron-depletion layer by additional electron extraction from the conduction band under an oxidizing gas atmosphere and liberation of captured electrons to the conduction band under a reducing gas atmosphere, respectively. In addition, it is possible that contact of individual NFs provides further resistance due to the networked configuration of NFs. However, it is reasonable to assume that the contribution of this type of resistance is negligible in comparison to other sources of resistance. Combined resistance modulation from the above-mentioned two sources results in an overall resistance modulation that can be observed in pure SnO_2 NFs during supply and stoppage of analytes gas molecules; this is illustrated schematically in Figure 7a.

Another sensing mechanism in addition to the above-mentioned two mechanisms is likely to operate in RGO NS-loaded SnO_2 NFs. As schematically shown in Figure 7b, local *p*−*n* heterojunctions are created in RGO NS-loaded SnO_2 NFs. Because the loaded RGO NSs have a discrete configuration, main conduction will occur along continuous SnO_2 NFs, rather than along discrete RGO NSs. Under these circumstances, a potential will develop at *p*−*n* heterojunctions, whose barrier will be changed by adsorption or desorption of gas molecules, resulting in additional modulation of the total resistance of the NFs. In addition to this, loaded *p*-RGO NSs will receive electrons from adjacent SnO_2 nanograins, playing the role of an electron-absorption body, resulting in an increase in local resistive space in NFs. This would cause the SnO_2 NFs to be more resistive, intensifying resistance modulation. The other possibility is that discrete RGO NSs play a catalytic role in adsorption and dissociation of NO_2 gas. The above-mentioned additional sources of resistance modulation would increase the resistance of SnO_2 NFs, as evidenced in Figure S6 (Supporting Information). We expect that the thickness of the NF films will be nearly identical, regardless of the amount of RGO NSs, because we have used the same electrospinning conditions (electrospinning time, feed rate, applied voltage, and distance between the tip of the needle and the collector). The BET analysis revealed that the surface area of the RGO NS-loaded SnO_2 NFs was 7.0574 m^2/g (Figure S7, Supporting Information). In our previous paper, we reported the BET surface areas of the SnO_2 NFs.[60] Because there is no clear evidence that the surface area has been increased by the loading of RGO NSs, the increase of surface area cannot account for the enhancement of sensing behavior.

We found that sensor resistance reached a maximum value at 0.44 wt % RGO NSs, yielding the most pronounced resistance modulation. However, additional loading of RGO NSs decreased the gas responses. This is likely due to percolation over the critical RGO NSs content, resulting in the formation of a conducting channel. In this case, *p*-type RGO NSs would cover a considerable part of the SnO_2 surface, promoting interconnection of neighboring RGO NSs. Accordingly, hole current would flow through the continuous RGO layer, acting as a parallel resistance and thus reducing the total resistance. Similar percolation phenomenon was observed in ZnO

DOI: 10.1021/am5071656
ACS Appl. Mater. Interfaces 2015, 7, 3101−3109

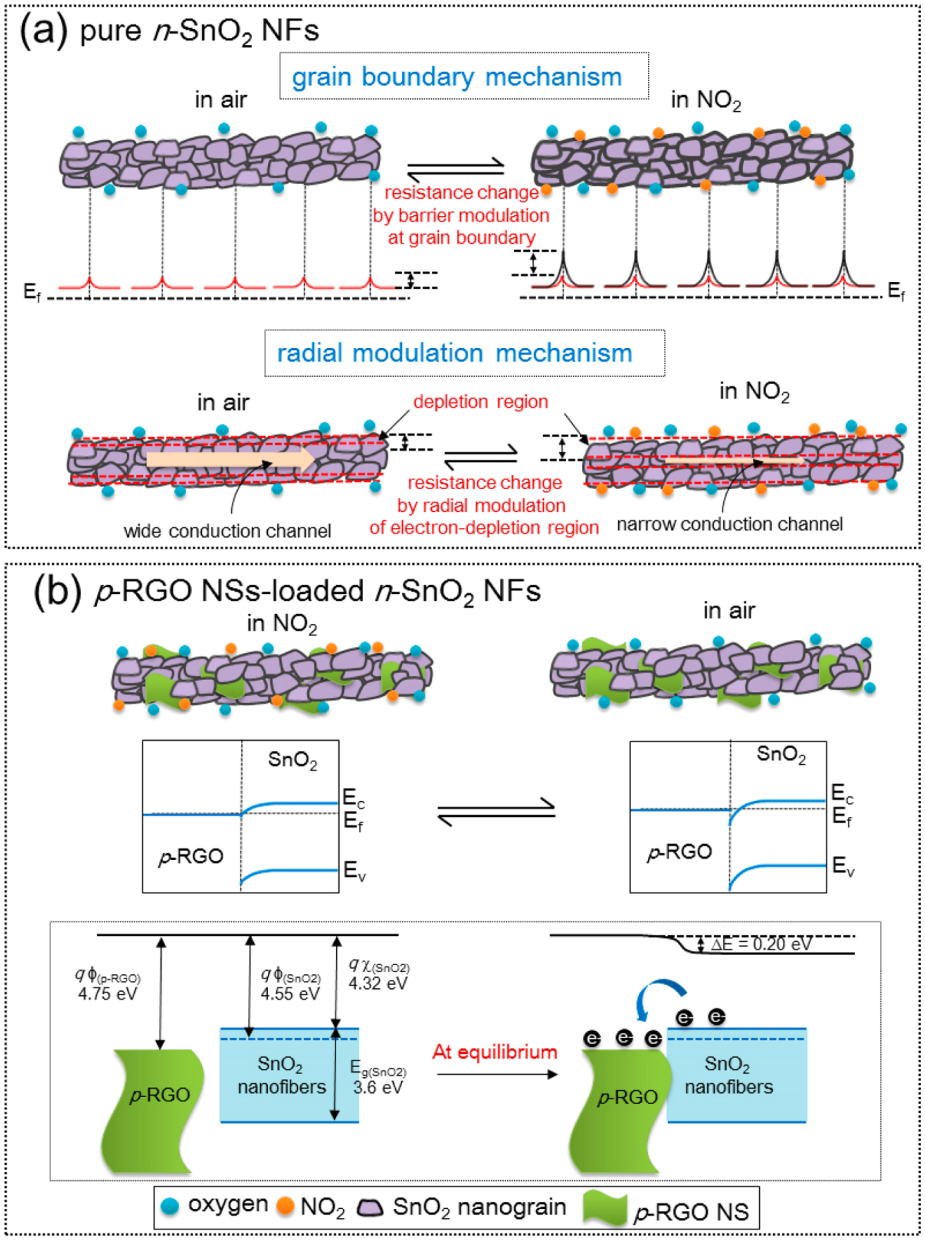

Figure 7. Schematic outlines of sensing mechanisms with respect to NO_2 gas, for (a) pure SnO_2 NFs and (b) RGO NSs-loaded SnO_2 NFs.

nanorods functionalized with spike-shaped CuO nanoparticles.[61] This overloading would therefore partially decrease the overall resistance of NFs, suppressing resistance modulation and resulting in lower gas responses.

5. CONCLUSIONS

In summary, we significantly enhanced the gas-sensing properties of *n*-type NFs by creating local *p*−*n* heterojunctions with *p*-type RGO NSs. SEM investigation revealed that the morphology, connectivity, and overall distribution of NFs were not dependent on the amount of loaded RGO NSs. The average diameter and nanograin size of NFs were about 180 and 30 nm, respectively, regardless of the amount of RGO NSs present. TEM investigation indicated that the loaded SnO_2 NFs were polycrystalline, and consisted of a significant quantity of nanograins. A NO_2 sensing test showed that the sensor response exhibited bell-shape behavior as a function of the amount of RGO NSs, as well as operating temperature. Sensor response was about 20-fold increased by loading an optimal amount of RGOs. We found that the sensor responses of the loaded SnO_2 NFs to reducing (oxidizing) gases, including H_2, CO, C_7H_8, and C_6H_6, (NO_2, O_2, and SO_2), were better than those of pure SnO_2 NFs. The sensing mechanism of pure SnO_2 NFs is related both to modulation of the potential barrier at nanograin boundaries and radial modulation of the electron-depletion layer. By loading *p*-RGO NSs into SnO_2 NFs, we obtained a higher sensing response, most likely due to the creation of local *p*−*n* heterojunctions that not only provided a potential barrier, but also played the role of a local electron absorption reservoir. While the sensor resistance was maximal at 0.44 wt % RGO NSs, further loading of RGO NSs decreased the gas responses, presumably due to percolation effects. The approach used in this work can be used to fabricate sensitive gas sensors based on *n*-type NFs.

DOI: 10.1021/am5071656
ACS Appl. Mater. Interfaces 2015, 7, 3101−3109

■ ASSOCIATED CONTENT

Supporting Information

Information for the determination of the content of the RGOs in the composite NFs; TEM images of RGO nanosheets; schematic diagram of the interdigital electrode pattern; TGA curves of RGO NS-loaded SnO_2 NFs and pure RGO NSs, SEM images of SnO_2 nanofibers; figures showing the sensor responses. This material is available free of charge via the Internet at http://pubs.acs.org.

■ AUTHOR INFORMATION

Corresponding Authors

*S. S. Kim. E-mail: sangsub@inha.ac.kr.

*H. W. Kim. E-mail: hyounwoo@hanyang.ac.kr.

Author Contributions

S.S.K. and H.W.K. conceived the study, designed the experiments and prepared the manuscript. J.-H.L., S.-W.C., A.K. and J.-H.K. performed the experiments. All authors approved the final version of the paper.

Notes

The authors declare no competing financial interest.

■ ACKNOWLEDGMENTS

This work was supported by a National Research Foundation of Korea (NRF) grant funded by the Korea government (MEST) (No. 2012R1A2A2A01013899).

■ REFERENCES

(1) Song, X.; Liu, L. Characterization of Electrospun ZnO−SnO_2 Nanofibers for Ethanol Sensor. *Sens. Actuators, A* **2009**, *154*, 175−179.

(2) Kolmakov, A.; Klenov, D. O.; Lilach, Y.; Stemmer, S.; Moskovits, M. Enhanced Gas Sensing by Individual SnO_2 Nanowires and Nanobelts Functionalized with Pd Catalyst Particles. *Nano Lett.* **2005**, *5*, 667−673.

(3) Zhou, J. Y.; Zhou, M.; Chen, Z. Y.; Zhang, Z. X.; Chen, C. C.; Li, R. S.; Gao, X. P.; Xie, E. Q. SiC Nanotubes Arrays Fabricated by Sputtering Using Electrospun PVP Nanofiber as Templates. *Surf. Coat. Technol.* **2009**, *203*, 3219−3223.

(4) Choi, J.-K.; Hwang, I.-S.; Kim, S.-J.; Park, J.-S.; Park, S.-S.; Jeong, U.; Kang, Y. C.; Lee, J.-H. Design of Selective Gas Sensors using Electrospun Pd-Doped SnO_2 Hollow Nanofibers. *Sens. Actuators, B* **2010**, *150*, 191−199.

(5) Wang, W.; Li, Z.; Liu, L.; Zhang, H.; Zheng, W.; Wang, Y.; Huang, H.; Wang, Z.; Wang, C. Humidity Sensor Based on LiCl-Doped ZnO Electrospun Nanofibers. *Sens. Actuators, B* **2009**, *141*, 404−409.

(6) Wang, Y. L.; Jiang, X. C.; Xia, Y. N. A Solution Phase Precursor Route to Polycrystalline SnO_2 Nanowires that Can Be Used for Gas Sensing under Ambient Conditions. *J. Am. Chem. Soc.* **2003**, *125*, 16176−16177.

(7) Cheng, L.; Ma, S. Y.; Li, X. B.; Luo, J.; Li, W. Q.; Li, F. M.; Mao, Y. Z.; Wang, T. T.; Li, Y. F. Highly Sensitive Acetone Sensors Based on Y-Doped SnO_2 Prismatic Hollow Nanofibers Synthesized by Electrospinning. *Sens. Actuators, B* **2014**, *200*, 181−190.

(8) Xu, X. R.; Sun, J. H.; Zhang, H. N.; Wang, Z. J.; Dong, B.; Jiang, T. T.; Wang, W.; Li, Z. Y.; Wang, C. Effects of Al Doping on SnO_2 Nanofibers in Hydrogen Sensor. *Sens. Actuators, B* **2011**, *160*, 858−863.

(9) Dong, K.-Y.; Choi, J.-K.; Hwang, I.-S.; Lee, J.-W.; Kang, B. H.; Ham, D.-J.; Lee, J.-H.; Ju, B.-K. Enhanced H_2S Sensing Characteristics of Pt Doped SnO_2 Nanofibers Sensors with Micro Heater. *Sens. Actuators, B* **2011**, *157*, 154−161.

(10) Choi, S.-W.; Katoch, A.; Zhang, J.; Kim, S. S. Electrospun Nanofibers of CuO-SnO_2 Nanocomposites as Semiconductor Gas Sensors for H_2S Detection. *Sens. Actuators, B* **2013**, *176*, 585−591.

(11) Du, H. Y.; Wang, J.; Su, M. Y.; Yao, P. J.; Zheng, Y. G.; Yu, N. S. Formaldehyde Gas Sensors Based on SnO_2/In_2O_3 Hetero-Nanofibers by a Modified Double Jets Electrospinning Process. *Sens. Actuators, B* **2012**, *166*, 746−752.

(12) Qi, Q.; Zhao, J.; Xuan, R.-F.; Wang, P.-P.; Feng, L.-L.; Zhou, L.-J.; Wang, D.-J.; Li, G.-D. Sensitive Ethanol Sensors Fabricated from p-Type $La_{0.7}Sr_{0.3}FeO_3$ Nanoparticles and n-Type SnO_2 Nanofibers. *Sens. Actuators, B* **2014**, *191*, 659−665.

(13) Basu, S.; Dutta, A. Modified Heterojunctions Based on Zinc Oxide Thin Film for Hydrogen Gas-Sensor Applications. *Sens. Actuators, B* **1994**, *22*, 83−87.

(14) Ushio, Y.; Miyayama, M.; Yanagida, H. Effects of Interface States on Gas-Sensing Properties of a CuO/ZnO Thin-Film Heterojunction. *Sens. Actuators, B* **1994**, *17*, 221−226.

(15) Ling, Z.; Leach, C.; Freer, R. Heterojunction Gas Sensors for Environmental NO_2 and CO_2 Monitoring. *J. Eur. Ceram. Soc.* **2001**, *21*, 1977−1980.

(16) Hu, Y.; Zhou, X.; Han, Q.; Cao, Q.; Huang, Y. Sensing Properties of CuO-ZnO Heterojunction Gas Sensors. *Mater. Sci. Eng.* **2003**, *B 99*, 41−43.

(17) Mridha, S.; Basak, D. Investigation of a *p*-CuO/n-ZnO Thin Film Heterojunction for H_2 Gas-Sensor Applications. *Semicond. Sci. Technol.* **2006**, *21*, 928−932.

(18) Huang, H.; Gong, H.; Chow, C. L.; Guo, J.; White, T. J.; Tse, M. S.; Tan, O. K. Low-Temperature Growth of SnO_2 Nanorod Arrays and Tunable n-p-n Sensing Response of a ZnO/SnO_2 Heterojunction for Exclusive Hydrogen Sensors. *Adv. Funct. Mater.* **2011**, *21*, 2680−2686.

(19) Ding, S.; Luan, D.; Boey, F. Y. C.; Chen, J. S.; Lou, X. W. SnO_2 Nanosheets Grown on Graphene Sheets with Enhanced Lithium Storage Properties. *Chem. Commun.* **2011**, *47*, 7155−7157.

(20) Robinson, J. T.; Perkins, F. K.; Snow, E. S.; Wei, Z.; Sheehan, P. E. Reduced Graphene Oxide Molecular Sensors. *Nano Lett.* **2008**, *8*, 3137−3140.

(21) Lu, G.; Ocola, L. E.; Chen, J. H. Reduced Graphene Oxide for Room-Temperature Gas Sensors. *Nanotechnology* **2009**, *20*, 445502.

(22) Dua, V.; Surwade, S. P.; Ammu, S.; Agnihorta, S. R.; Jain, S.; Roberts, K. E.; Park, S.; Ruoff, R. S.; Manohar, S. K. All-Organic Vapor Sensor using Inkjet-Printed Reduced Graphene Oxide. *Angew. Chem., Int. Ed.* **2010**, *49*, 2154−2157.

(23) Deng, S.; Tjoa, V.; Fan, H. M.; Tan, H. R.; Sayle, D. C.; Olivo, M.; Mhaisalkar, S.; Wei, J.; Sow, C. H. Reduced Graphene Oxide Conjugated Cu_2O Nanowire Mesocrystals for High Performance NO_2 Gas Sensor. *J. Am. Chem. Soc.* **2012**, *134*, 4905−4917.

(24) Liang, R. L.; Cao, H. Q.; Qian, D.; Zhang, J. X.; Qu, M. Z. Designed Synthesis of SnO_2-Polyaniline-Reduced Graphene Oxide Nanocomposites as an Anode Material for Lithium-Ion Batteries. *J. Mater. Chem.* **2011**, *21*, 17654−17657.

(25) Zhang, M.; Lei, D.; Du, Z. F.; Yin, X. M.; Chen, L. B.; Li, Q. H.; Wang, Y. G.; Wang, T. H. Fast Synthesis of SnO_2/Graphene Composites by Reducing Graphene Oxide with Stannous Ions. *J. Mater. Chem.* **2011**, *21*, 1673−1676.

(26) Wei, Y.; Gao, C.; Meng, F. L.; Li, H. H.; Wang, L.; Liu, J. H.; Huang, X. J. SnO_2/Reduced Oxide Nanocomposite for the Simultaneous Electrochemical Detection of Cadmium(II), Lead(II), Copper(II), and Mercury(II): An Interesting Favorable Mutual Interference. *J. Phys. Chem. C* **2012**, *116*, 1034−1041.

(27) Neri, G.; Leonardi, S. G.; Latino, M.; Donato, N.; Baek, S.; Conte, D. E.; Russo, P. A.; Pinna, N. Sensing Behavior of SnO_2/Reduced Graphene Oxide Nanocomposites toward NO_2. *Sens. Actuators, B* **2013**, *179*, 61−68.

(28) Chen, M. X.; Zhang, C. C.; Li, L. Z.; Liu, Y.; Li, X. C.; Xu, X. Y.; Xia, F. L.; Wang, W.; Gao, J. P. Sn Powder as Reducing Agents and SnO_2 Precursors for the Synthesis of SnO_2-Reduced Graphene Oxide Hybrid Nanoparticles. *ACS Appl. Mater. Interfaces* **2013**, *5*, 13333−13339.

(29) Zhang, H.; Feng, J.; Fei, T.; Liu, S.; Zhang, T. SnO_2 Nanoparticles-Reduced Graphene Oxide Nanocomposites for NO_2 Sensing at Low Operating Temperature. *Sens. Actuators, B* **2014**, *190*, 472−478.

DOI: 10.1021/am5071656
ACS Appl. Mater. Interfaces 2015, 7, 3101−3109

(30) Wang, Y.-X.; Lim, Y.-G.; Park, M.-S.; Chou, S.-L.; Kim, J. H.; Liu, H.-K.; Dou, S.-X.; Kim, Y.-J. Ultrafine SnO_2 Nanoparticle Loading onto Reduced Graphene Oxide as Anodes for Sodium-Ion Batteries with Superior Rate and Cycling Performances. *J. Mater. Chem. A* **2014**, *2*, 529−534.
(31) Guo, J.; Jiang, B.; Zhang, X.; Liu, H. Monodisperse SnO_2 Anchored Reduced Graphene Oxide nanocomposites as Negative Electrode with High Rate Capability and Long Cyclability for Lithium-Ion Batteries. *J. Power Sources* **2014**, *262*, 15−22.
(32) Dutta, D.; Chandra, S.; Swain, A. K.; Bahadur, D. SnO_2 Quantum Dots-Reduced Graphene Oxide Composite for Enzyme-Free Ultrasensitive Electrochemical Detection of Urea. *Anal. Chem.* **2014**, *86*, 5914−5921.
(33) Ye, Y.; Wang, P.; Dai, E.; Liu, J.; Tian, Z.; Liang, C.; Shao, G. A Novel Reduction Approach to Fabricate Quantum-Sized SnO_2-Conjugated Reduced Graphene Oxide Nanocomposites as Non-enzymatic Glucose Sensors. *Phys. Chem. Chem. Phys.* **2014**, *16*, 8801−8807.
(34) Li, L.; Kovalchuk, A.; Tour, J. M. SnO_2-Reduced Graphene Oxide Nanoribbons as Anodes for Lithium Ion Batteries with Enhanced Cycling Stability. *Nano Res.* **2014**, *7*, 1319−1326.
(35) Choi, S.-J.; Jang, B.-H.; Lee, S.-J.; Min, B. K.; Rothschild, A.; Kim, I.-D. Selctive Detection of Acetone and Hydrogen Sulfide for the Diagnosis of Diabetes and Halitosis Using SnO_2 Nanofibers Functionalized with Reduced Graphene Oxide Nanosheets. *ACS Appl. Mater. Interfaces* **2014**, *6*, 2588−2597.
(36) Stankovich, S.; Dikin, D. A.; Piner, R. D.; Kohlhaas, K. A.; Kleinhammes, A.; Jia, Y.; Wu, Y.; Nguten, S. T.; Ruoff, R. S. Synthesis of Graphene-based Nanosheets via Chemical Reduction of Exfoliated Graphite Oxide. *Carbon* **2007**, *45*, 1558−1565.
(37) Cui, P.; Lee, J.; Hwang, E.; Lee, H. One-Pot Reduction of Graphene Oxide at Subzero Temperatures. *Chem. Commun.* **2011**, *47*, 12370−12372.
(38) Katoch, A.; Byun, J.-H.; Choi, S.-W. One-Pot Synthesis of Au-Loaded SnO_2 Nanofibers and Their Gas Sensing Properties. *Sens. Actuators B* **2014**, *202*, 38−45.
(39) Zhu, J.; Lu, Z.; Aruna, S. T.; Aurbach, D.; Gedanken, A. Sonochemical Synthesis of SnO_2 Nanoparticles and Their Preliminary Study as Li Insertion Electrodes. *Chem. Mater.* **2000**, *12*, 2557−2566.
(40) Choi, S. W.; Park, J. Y.; Kim, S. S. Synthesis of SnO_2−ZnO Core−Shell Nanofibers via a Novel Two-Step Process and Their Gas Sensing Properties. *Nanotechnology* **2009**, *20*, 465603−465608.
(41) Park, J. Y.; Choi, S. W.; Lee, J. W.; Lee, C.; Kim, S. S. Synthesis and Gas Sensing Properties of TiO_2−ZnO Core-Shell Nanofibers. *J. Am. Ceram. Soc.* **2009**, *92*, 2551−2554.
(42) Kim, H. W.; Shim, S. H.; Lee, J. W.; Park, J. Y.; Kim, S. S. $Bi_2Sn_2O_7$ Nanoparticles Attached to SnO_2 Nanowires and Used as Catalysts. *Chem. Phys. Lett.* **2008**, *456*, 193−197.
(43) Park, J. Y.; Choi, S. W.; Kim, S. S. Fabrication of a Highly Sensitive Chemical Sensor Based on ZnO Nanorod Arrays. *Nanoscale Res. Lett.* **2010**, *5*, 353−359.
(44) Choi, S.-W.; Park, J. Y.; Kim, S. S. Growth Behavior of Sensing Properties of Nanograins in CuO Nanofibers. *Chem. Eng. J.* **2011**, *172*, 550−556.
(45) Park, J. Y.; Asokan, K.; Choi, S.-W.; Kim, S. S. Growth Kinetics of Nanograins in SnO_2 Fibers and Size Dependent Sensing Properties. *Sens. Actuators, B* **2011**, *152*, 254−260.
(46) Park, J. Y.; Kim, S. Growth of Nanograins in Electrospun ZnO Nanofibers. *J. Am. Ceram. Soc.* **2009**, *92*, 1691−1694.
(47) Rahaman, M. N. *Ceramic Processing and Sintering*; Marcel Dekkar Inc: New York, 1995.
(48) Lim, S. K.; Hwang, S.-H; Chang, D.; Kim, S. Preparation of Mesoporous In_2O_3 Nanofibers by Electrospinning and Their Application as a CO Gas Sensor. *Sens. Actuators, B* **2010**, *149*, 28−33.
(49) Leng, J. Y.; Xu, X.-J.; Lv, N.; Fan, H.-T.; Zhang, T. J. Synthesis and Gas-Sensing Characteristics of WO_3 Nanofibers via Electrospinning. *J. Colloid Interface Sci.* **2011**, *356*, 54−57.
(50) Viter, R.; Katoch, A.; Kim, S. S. Grain Size Dependent Bandgap Shift of SnO_2 Nanofibers. *Met. Mater. Int.* **2014**, *20*, 163−167.
(51) Wang, Y.; Ramos, I.; Santiago-Aviles, J. J. Optical Bandgap and Photoconductance of Electrospun Tin Oxide Nanofibers. *J. Appl. Phys.* **2007**, *102*, 093517.
(52) Barakat, N. A. M.; Khil, M. S.; Sheikh, F. A.; Kim, H. Y. Synthesis and Optical Properties of Two Cobalt Oxides (CoO and Co_3O_4) Nanofibers Produced by Electrospinning Process. *J. Phys. Chem. C* **2008**, *112*, 12225−12233.
(53) Qi, S.; Zuo, R.; Liu, Y.; Wang, Y. Synthesis and Photocatalytic Activity of Electrospun Niobium Oxide Nanofibers. *Mater. Res. Bull.* **2013**, *48*, 1213−1217.
(54) Song, J. H.; Nam, J. H.; Cho, J. H.; Kim, B. I.; Chun, M. P. Microstructures and Multiferroic Properties of Electrospun $BiFeO_3$ Nanofibers. *J. Korean Phys. Soc.* **2011**, *59*, 2308−2312.
(55) Zhang, J.; Fu, J.; Li, F.; Xie, E.; Xue, D.; Mellors, N. J.; Peng, Y. $BaFe_{12}O_{19}$ Single-Particle-Chain Nanofibers: Preparation, Characterization, Formation Principle, and Magnetization Reversal Mechanism. *ACS Nano* **2012**, *6*, 2273−2280.
(56) Liu, M.; Shen, X.; Song, F.; Xiang, J.; Meng, X. One-Dimensional $SrFe_{12}O_{19}/SrSiO_3$ Composite Nanofibers: Preparation, Structure and Magnetic Properties. *Mater. Chem. Phys.* **2010**, *124*, 970−975.
(57) Kozhushner, M. A.; Trakhtenberg, L. I.; Bodneva, V. L.; Belisheva, T. V.; Landerville, A. C.; Oleynik, I. L. Effect of Temperature and Nanoparticle Size on Sensor Properties of Nanostructures Tin Oxide Films. *J. Phys. Chem. C* **2014**, *118*, 11440−11444.
(58) Chen, M.; Wang, Z.; Han, D.; Gu, F.; Guo, G. High-Sensitivity NO_2 Gas Sensors Based on Flower-like and Tube-like ZnO Nanomaterials. *Sens. Actuators, B* **2011**, *157*, 565−574.
(59) Teoh, L. G.; Hung, I. M.; Shieh, J.; Lai, W. H.; Hon, M. H. High Sensitivity Semiconductor NO_2 Gas Sensor Based on Mesoporous WO_3 Thin Film. *Electrochem. Solid-Stat. Lett.* **2003**, *6*, G108−G111.
(60) Choi, S.-W.; Zhang, J.; Akash, K.; Kim, S. S. H_2S Sensing Performance of Electrospun CuO-Loaded SnO_2 Nanofibers. *Sens. Actuators, B* **2012**, *169*, 54−60.
(61) Rai, P.; Jeon, S.-H.; Lee, C.-H.; Lee, J.-H.; Yu, Y.-T. Functionalization of ZnO Nanorods by CuO Nanospikes for Gas Sensor Applications. *RSC Adv.* **2014**, *4*, 23604−23609.

DOI: 10.1021/am5071656
ACS Appl. Mater. Interfaces 2015, 7, 3101−3109